

Visualizing the merger of tunably coupled graphene quantum dots

Daniel Walkup^{1,*}, Fereshte Ghahari^{1,2,*}, Steven R. Blankenship¹, Kenji Watanabe³, Takashi Taniguchi⁴, Nikolai B. Zhitenev¹ and Joseph A. Stroscio¹

¹*Physical Measurement Laboratory, National Institute of Standards and Technology, Gaithersburg, Maryland 20899, USA*

²*Department of Physics, George Mason University, Fairfax, Virginia 22030, USA*

³*Research Center for Electronic and Optical Materials, National Institute for Materials Science; 1-1 Namiki, Tsukuba, Ibaraki 305-0044, Japan*

⁴*Research Center for Materials Nanoarchitectonics, National Institute for Materials Science; 1-1 Namiki, Tsukuba, Ibaraki 305-0044, Japan*

 (Received 23 June 2023; revised 6 October 2023; accepted 13 November 2023; published 6 December 2023)

We examine graphene quantum dots in back-gated devices on hexagonal boron nitride (hBN) and visualize their merger using scanning tunneling microscopy (STM) and scanning tunneling spectroscopy. These dots are formed by the combination of nanoscale potential wells created by pulsing the voltage of an STM tip above charged defects in the hBN underlayer, and strong magnetic fields gapping the density of states, which add insulating rings in the potential wells. Control of the charge state is achieved via the back gate and sample bias voltages, and the position of the STM tip which serves as a mobile top gate. The individual quantum dots present a distinct phenomenology of single-electron charging due to multiple Landau levels crossing the Fermi energy concentrically. Here, we study side by side pairs of these quantum dots via STM, where we observe a tunable interdot coupling and mergeability. Specifically, with increasing charge filling, the quantum dots formed by electrons belonging to one Landau level merge into a single quantum dot, while the electrons in the next-higher Landau level remain spatially separated into two charge pockets. Using the probe tip as a multifunction tool, we visualize the evolution, growth, and merger of this unique double quantum dot system as a function of tip position and gate voltages.

DOI: [10.1103/PhysRevB.108.235407](https://doi.org/10.1103/PhysRevB.108.235407)

I. INTRODUCTION

In recent years, defect charging in hBN has proved a versatile avenue to controlling charge density and potential landscape in graphene devices, thus forming structures with novel electronic properties [1–6]. When the charging is achieved via electric fields enhanced by the end of a scanning probe tip, the doping is concentrated in nanoscale pockets, and the resulting potential wells display intriguing phenomena which greatly depend on the magnetic field strength. When the magnetic length is comparable to the well size, the semi-classical orbits are bent, leading to a discontinuous shift of the quantum state energies as a function of the field [7–9]. At stronger fields, Landau levels become apparent in the density of states, and wedding-cake-like structure of alternating compressible-incompressible quantum Hall states form because of electron interactions [10]. At yet stronger fields, the gaps between Landau levels give rise to insulating behavior between the pinning rings, creating islands with quantized charge [11]. Adding to the complexity, under certain conditions more than one successive Landau level will be filled within the dot, creating a type of concentric double quantum dot (DQD) within a single potential well, with unique single-electron charging properties [11]. Unlike the better-known semiconductor DQDs where the barrier is formed by a gate-

tunable constriction [12,13], this DQD cannot be merged by electrostatic means but only by turning off the magnetic field, which destroys the insulating barriers altogether.

Here, by contrast, we describe double quantum dots consisting of adjacent potential wells of the type described in [11], constructed in the same back-gated graphene device (Fig. 1). Although each single dot retains the concentricity features of [11], the double-dot system as a whole possesses the electrostatically tunable coupling associated with the classic DQD systems in ordinary semiconductors (Fig. 2), where the gating in the constriction tunes between separate dots with small tunnel coupling, and a stadium-shaped merged single dot. But compared to those systems, there is the additional differentiation that our imaging and charge-sensing tool, the scanning tunneling microscopy (STM) tip, is a strong source of gating for the dots [14,15], which disturbs the potential and produces concentric series of charging rings in tip scans, similar to the images obtained in scanning gate microscopy [16]. The resulting experimental system is very feature-rich, but requires careful analysis to extract meaningful physical conclusions.

II. RESULTS

The data presented here are the differential tunneling conductance, dI/dV , signals acquired from the STM tunneling current, using the standard lock-in technique. Under certain frequently encountered conditions dI/dV is proportional to the sample's local density of states [17,18], but in experiments

*These authors contributed equally to this work.

†daniel.walkup@nist.gov

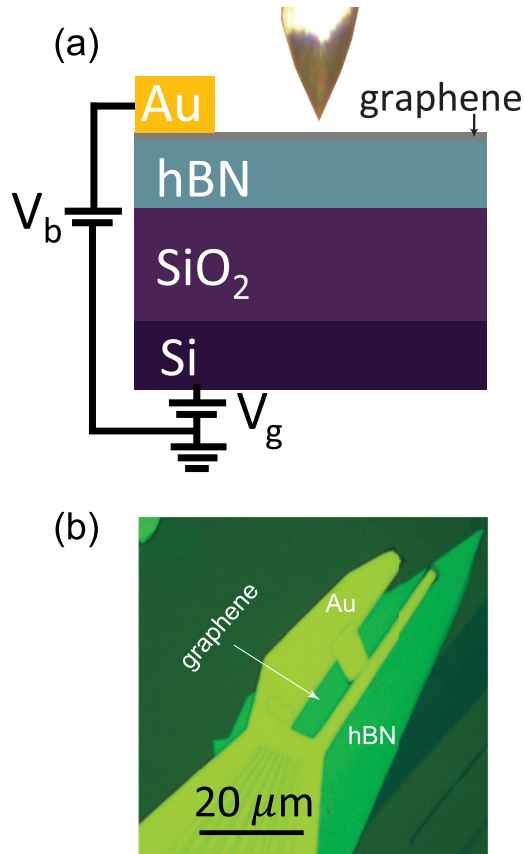


FIG. 1. Back-gated graphene device used to create the double quantum dot. (a) Cross-sectional view of the graphene device including STM tip. (b) Optical microscope image of the device; bright green is hBN, yellow is the Au landing pad.

on semiconducting systems containing chargeable defects, the charging creates additional contributions to the dI/dV signal, in the form of sharp peaks or rings at the threshold loci, where the defect charge state changes as a function of tip position, bias, or gate voltage [15,19–21]. These signatures arise from the sudden change in the local density of states underneath the tip, due to changes in screening when the defect is charged or discharged. In this situation, the tunnel current develops an exquisite sensitivity to the electrostatic state of the sample, somewhat analogous to that of the quantum point contact in fixed-gate DQD experiments (e.g., [22]). Thus the tip here plays the multiple roles of mobile top gate, current lead (with currents on the order of 100 pA), and charge sensor.

Figure 3 shows STM dI/dV data on a p -type DQD. Figure 3(a) is a topographic height map of the area containing the quantum dots, at $B = 0$. The graphene lattice is pristine over the double-dot landscape and the only significant topographic features are ≈ 20 nm “hills” a few angstroms tall, which have no apparent correlation with the potential landscape and are likely due to the roughness of the SiO_2 substrate, and is smoothed by the ≈ 30 nm hBN underlayer. Two p -type potential wells were fashioned in this area using the method described in [1], near the centers of the dashed circles. At $B = 8$ T, STM scans [Figs. 3(b)–3(h)] show multiple series of concentric charging rings, where the peak positions depend systematically on tunneling sample bias, V_b , and back-gate

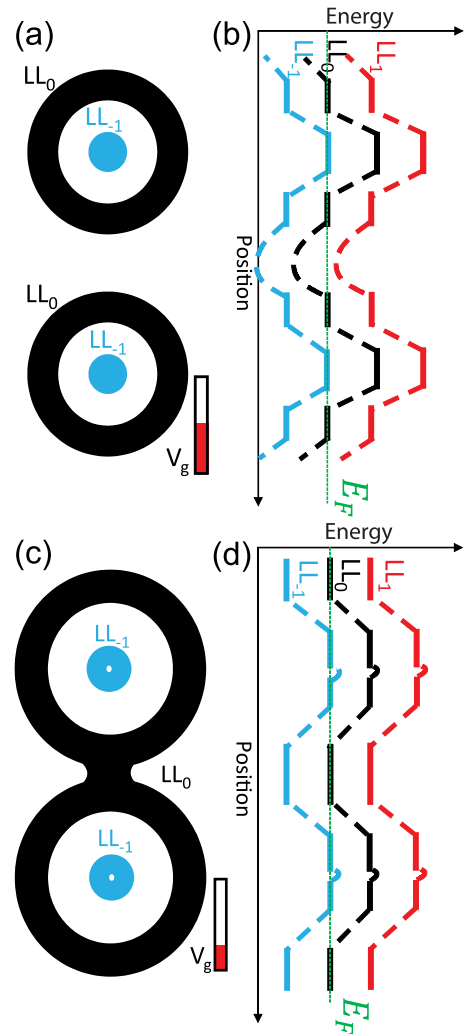


FIG. 2. Schematic of the graphene Landau level double quantum dot (DQD). (a), (c) Top-view schematics showing the compressible areas where labeled Landau levels cross the Fermi energy, with gate voltage decreasing from (a) to (c) in a p -type potential well. (b), (d) Energy-displacement schematic through the center of the two dots. The Y axis of (b), (d) is aligned with that of (a), (c), and the latter represent the Fermi-energy slices of the energy diagrams (b), (d) respectively. The islands formed by the $N = 0$ Landau level merge between (a) and (c), and (b) and (d).

voltage V_g . In p -type QD wells the Landau levels are concave down in an energy-position plot, and the dot consists of the unoccupied region of the Landau level, where the well potential pulls it above the Fermi energy [Figs. 2(b) and 2(d)] [10,11]. As the back-gate potential V_g decreases, the Landau levels rise above the Fermi level which increases the lateral size of the unoccupied hole states (Fig. 2). This larger size decreases the spacing between consecutive charging peaks in the dI/dV versus V_g measurements [Fig. 3(i)] [11].

To investigate the DQD system in detail, we acquired a dense three-dimensional dataset of dI/dV in the DQD as a function of the lateral tip position (X and Y) and V_g , at fixed V_b and tunnel current, which is exhibited in Figs. 3(b)–3(i). At high V_g it is apparent that the charging peaks, which take the form of annular rings about each well center, can be ascribed

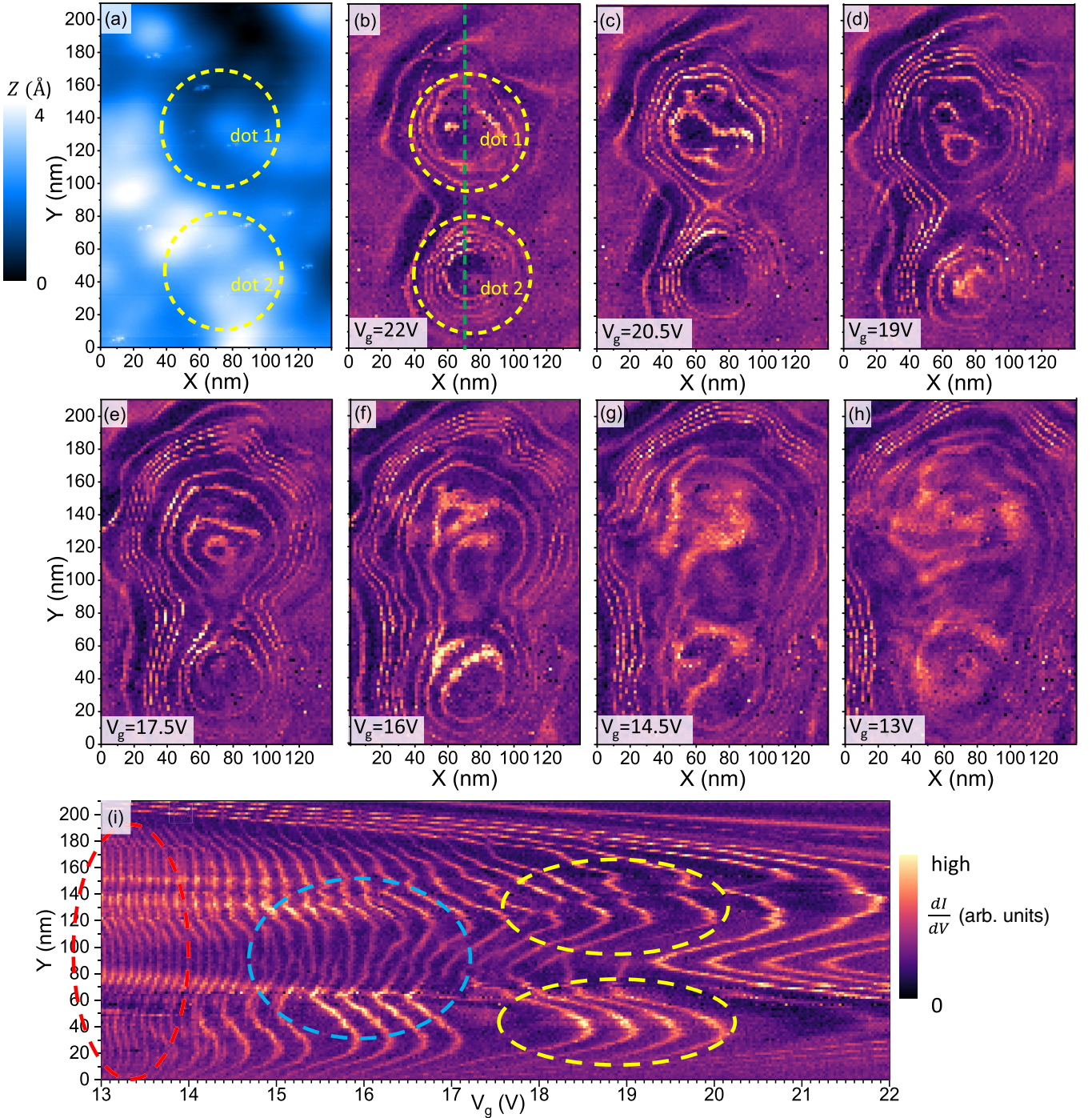


FIG. 3. Spatial tunneling measurements of a graphene double quantum dot (DQD). (a) STM topography showing the area of the graphene DQD at zero magnetic field. Tunneling set point: Current $I = 50$ pA, $V_b = -100$ mV, $V_g = 12$ V. (b)–(h) Spatial map of the dI/dV signal in the DQD at fixed sample bias $V_b = -150$ mV and gate voltage V_g indicated in each panel. As the tip gates the dots, concentric rings correspond to single-electron charging events. The dashed yellow circles in (b) outline the areas of dot 1 and dot 2. Tunneling set point: Current $I = 80$ pA, $V_b = -150$ mV. (i) Series of dI/dV versus V_g curves as a function of the Y-axis tip position along the green dashed line at $X = 70$ nm in (b) and the same fixed sample bias. The regions of separate dots, coupled dots, and a merged dot are indicated by yellow, blue, and red ovals, respectively. Temperature $T = 4.3$ K in all panels, magnetic field, $B = 8$ T in panels (b)–(i).

to one dot or the other [Figs. 3(c) and 3(d)]. The sole exception is a single quartet of charging rings, visible along the top and right edges of Fig. 3(i), related to a small quantum dot induced by tip gating which is observed even in graphene without QDs [11,23]. These do not form part of the series of DQD charging

lines, and are not relevant to the present discussion. As V_g decreases, the situation becomes more complex; for example, in Fig. 3(e) the charging rings of the upper dot seem to blur as they approach the lower dot, while others seem to encompass the whole dot like a stadium. At still lower V_g , [Figs. 3(g)

and 3(h)] the charging features in the interior of each dot meander and are no longer concentric. Each charging peak seems smeared out over the large parts of the DQD and one can hardly distinguish the individual peaks (see Supplemental Material [24]).

To better visualize the evolution of the DQD, we slice this dataset in the V_g - Y plane producing Fig. 3(i). Here the charging rings in the top view plots appear as curves which are mostly concave to the left, and three regions are readily distinguishable: (1) the high- V_g regime where each curve is concave within one dot and does not penetrate the other dot (two yellow ovals); (2) a transitional regime in which the charging curves still decrease in intensity between dots, but interleaving of the lines is readily apparent (blue oval); (3) a regime of dense charging curves which seem to occupy the whole DQD, with a spacing that is even and almost uniform as a function of position within the DQD (red oval). This increasing parallelism and indistinguishability of consecutive charging lines is a clear indicator of a merged quantum dot [12,25,26]. In what follows, we will relate the physical parameters of our DQD as extracted from these charging curves to the theoretical models [25,26], which are tunable between strongly coupled dots and a merged “single” dot (reached in the strong-coupling limit).

To extract more quantitative information, we systematically swept V_g and V_b along a dense sequence of spatial points through the DQD (Fig. 4). Figure 4(a) shows the dI/dV measurement in the Y versus V_g plane at $V_b = -150$ mV, for comparison with Fig. 3(i). Figures 4(b)–4(f) shows the corresponding V_b versus V_g maps at the points indicated in Fig. 4(a), moving from dot 2 up toward dot 1. Similar to measurements on DQDs with fixed gates, in the voltage-voltage plots the “charging curves” from the top views of the DQD [Figs. 3(b)–3(i)] become lines with definite slopes, which indicate the relative capacitance between the gate electrodes and the dot whose constant-charge condition the charging line represents. These lines divide the V_g - V_b plane into stretched hexagonal cells [see features in blue circle in Fig. 4(d), for example], within which each element of the DQD contains a definite number of electrons (N_1, N_2). Here, the Landau levels appear as increased intensity in nearly horizontal lines or strips which are gradually pulled down to lower tunneling energies by increasing back-gate voltage, as indicated by green dashed lines in Fig. 4(b). The single-electron charging peaks from the dots have positive slope, because V_b is applied to the sample rather than the virtually grounded tip. Thus from the plots in Figs. 4(b)–4(f) we can obtain what amounts to experimentally derived charge stability diagrams for the DQD. The blue circle in Fig. 4(d) shows a representative cluster of hexagonal cells in the weak-coupling regime [see also Fig. 5(a)]. As we move to the left and the interdot coupling strengthens with decreasing V_g , the “pinch points” of the hexagons [avoided crossing points, white arrows in Fig. 4(d)] at the lower-left and upper-right cell corners widen until, around $V_g = 14$ V, the two sets of lines become roughly parallel, evenly spaced, and indistinguishable [green circle in Fig. 4(d)]. An interesting observation is that the two sets of lines swap their relative slopes as we move from the lower dot to the upper dot between Figs. 4(b) and 4(f), with the crossover point occurring roughly at Fig. 4(e).

Before trying to extract quantitative dot parameters from these charge stability diagrams, let us make some qualitative remarks about the slope of the charging lines and its physical significance [11,25]. Because the charging line represents a constant-charge condition of one of the quantum dots, its slope in the V_g - V_b plane reveals the relative capacitance of the gate electrodes, in this case the Si back gate and the STM tip. As the tip moves away from the dot, the tip-dot capacitance decreases, and a greater amount of voltage needs to be applied to counteract an incremental voltage on the back gate; the slope goes up as we move away from the bottom dot. Therefore, in Fig. 4(f) where the tip is closest to dot 1, we can confidently assert that the steeper and fainter group of charging lines belongs to dot 2, and vice versa: moving the tip back toward dot 2 steepens the charging lines of dot 1. In addition to changing the slope, charging lines in the weak-coupling regime also fade in intensity as the tip moves away from the corresponding dot [Fig. 4(a)], confirming our physical intuition regarding their relative slope. To help the reader visualize the hexagonal cells, yellow and cyan dashed lines are included in Figs. 4(d) and 4(f) as guides to the eye for the charging lines of dots 1 and 2, respectively, as well as white arrows indicating the corners of the hexagons, which open up with increasing interdot coupling.

III. DISCUSSION

Our attempts to extract quantitative dot parameters from the observed charging line avoided crossings are based on the models described in Refs. [25–28]. Reference [25] describes a model which regards each dot as a metal island connected to the gate electrodes and the other dot by capacitor plates. Ignoring quantum-mechanical terms in the addition energy, the charging energies of each dot are calculated electrostatically in terms of the dot capacitances: $E_{C_i} = \frac{e^2}{C_i} \left(1 - \frac{C_m^2}{C_1 C_2}\right)^{-1}$ where i is the dot index, C_i is the sum of all capacitances connected to the i th dot, and C_m is the interdot capacitance. The interdot capacitance leads to a mutual charging energy $E_{C_m} = \frac{e^2}{C_m} \left(\frac{C_1 C_2}{C_m^2} - 1\right)^{-1}$. It follows from $C_m < C_i$ that $E_{C_m} < E_{C_i}$. The limit of merged dots corresponds to $C_m \gg$ all other electrode capacitances, so that $C_1 \approx C_2 \approx C_m$ and $E_{C_1} \approx E_{C_2} \approx E_{C_m}$. This equalization of the charging energies is retained in the Hubbard-model treatments [26,28,29], which discard the unphysical infinite increase of C_m and typically label the charging energies U_1, U_2 , and U_{12} , respectively. In addition to electrostatic coupling, the Hubbard models allow for tunnel coupling in the form of a hopping energy t . In the theoretical charge stability diagrams of either model, at zero coupling the charging lines form a grid of parallelograms with respect to N_1 and N_2 . Finite U_{12} or E_{C_m} splits two corners of each parallelogram, making hexagons with open faces between adjoining cells with the same total charge count $N_1 + N_2$. The Hubbard-model t term introduces curvature in the charging lines at these corners, and together with U_{12} converts the grid of hexagons into a pattern of roughly parallel wavy lines [26,28]. In both models the positions of the charging lines are determined by chemical potentials μ_i , which are obtained from the gate voltages using capacitive lever arms.

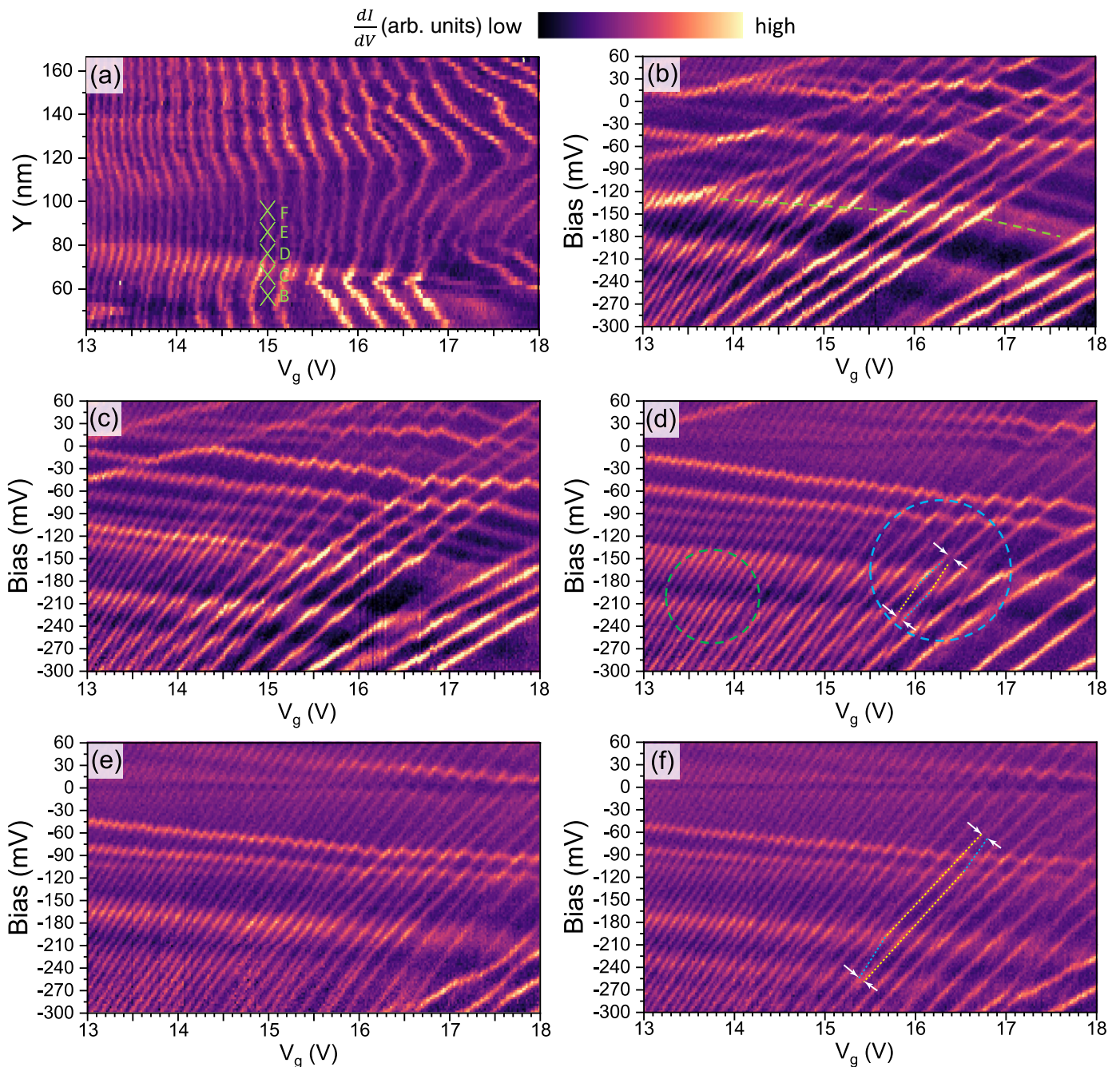


FIG. 4. Single-electron charging measurements of the double quantum dot. (a) Series of dI/dV versus V_g curves as a function of the Y -axis tip position obtained in the center of the dot at $X = 70$ nm in Fig. 3(b) and fixed sample bias $V_b = -150$ mV. (b)–(f) dI/dV measurements in the V_b, V_g plane at the tip positions indicated by green \times 's in (a). Moving from (b) to (f) up the Y axis, the tip departs dot 2 and moves toward dot 1, with corresponding changes in the slopes of the two series of charging lines belonging to dot 1 and dot 2 [yellow and cyan dashed lines, respectively, in (d), (f)]. Avoided crossings are visible, illustrated by the arrows in (d), (f). Regions of weakly coupled dots and nearly merged dots are circled in blue and green in (d), respectively. Tunneling set point: Current $I = 150$ pA, $V_b = 300$ mV. Temperature $T = 4.3$ K, magnetic field, $B = 8$ T.

For our datasets, the observed curvature is insufficiently resolved to reliably estimate the hopping parameter (which in any case is often small compared to U_{12} [26,28]), so we omitted it here. In this regime a full reconstruction of the Hubbard model would involve seven parameters: the capacitances between the two gates and each dot, U_i , and U_{12} . Equivalently, within the capacitor model one would also have the four gate-dot capacitances, C_m , and an unknown additional

capacitance between each dot and the rest of the universe, making seven parameters total; U_i and U_{12} would be derived quantities—but regardless of the choice of model, the hexagonal cell of the charge stability diagram has only six degrees of freedom. Empirically and algebraically (see Appendix B), we found that by fitting within the capacitance model we can obtain reliable estimates for the four dot-gate capacitances and the two ratios U_{12}/U_i . The seventh free

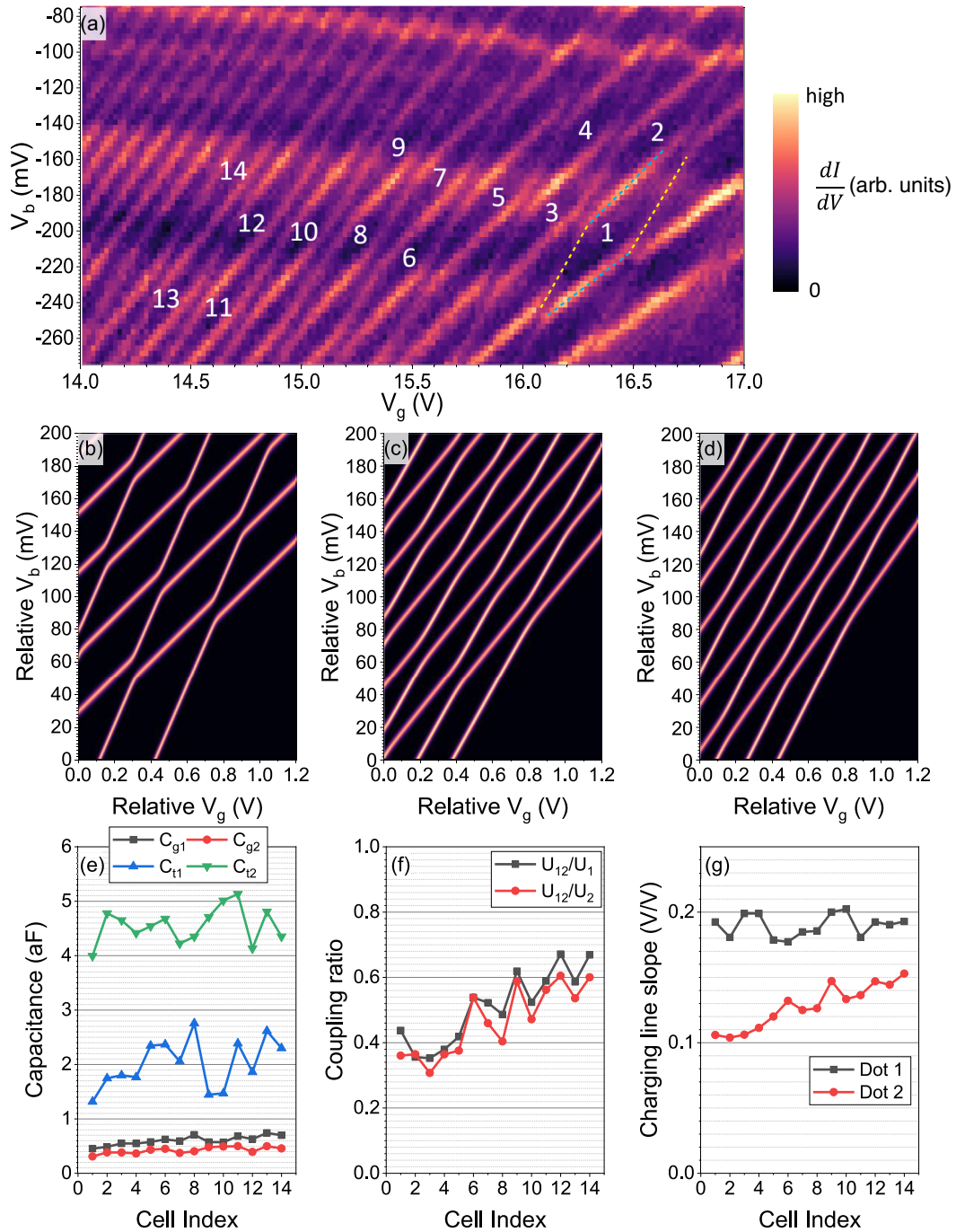


FIG. 5. Model calculations for charge stability diagrams of the double quantum dot DQD. (a) An expanded section of data in Fig. 3(d), with labels indicating the hexagonal cells whose dimensions were used to estimate capacitances and to generate the simulated charge-stability diagram of a fixed-size DQD in (b)–(d). The diagrams show the lines becoming more parallel in going from (b) to (d), indicating the increased interdot coupling (f). The panels (b)–(d) use capacitances estimated from cells labeled 1, 6, and 14 in (a), respectively. The estimated model parameters are shown in (e), (f) and the slopes of the charging lines are shown in (g).

parameter results in an unknown overall energy scale factor U , which is controlled by the three unknown capacitances including C_m .

Figure 5 shows the results of such model fittings for a contiguous series of 14 hexagonal cells extracted from the data in Fig. 4(d). The choice of the contiguous series, shown in Fig. 5(a), makes a zigzag path charge stability diagram in order to avoid going over the edges of the experimental

voltage range. The first cell having been designated arbitrarily as $(N_1, N_2) = (1, 1)$ [Fig. 5(b), white numerals in Fig. 5(a)], the sixth cell [Fig. 5(c)] is (4,3) and the 14th cell [Fig. 5(d)] is (8,7). (The fitting was stopped after 14 cells because the lines were too parallel to reliably identify the cell corners.) With increasing total charge count, the fitted coupling parameters U_{12}/U_i [Fig. 5(e)] show a general upward trend, consistent with expectations. The model-fitted capacitances also show

characteristic behavior. The tip capacitance of dot 2 [green curve in Fig. 5(e)], which is more closely underneath the tip at this position [position D in Fig. 4(a)], is more than twice that of dot 1 [blue curve in Fig. 5(e)], but dot 1, which is bigger than dot 2 at these voltages [see Figs. 3(e)–3(g)], has a larger capacitance to the back gate. Although the fitted capacitances fluctuate, possibly due to quantum energy effects [25], the fitted slopes are relatively stable and the upward trend in dot 2 is evident [Fig. 5(g)]. The relative flatness of dot 1's slope with the cell index in Fig. 5(g) compared to dot 2 can be attributed to the greater distance of dot 1 from the tip where this dataset was acquired [at position D in Fig. 4(a)]. At this greater distance the tip and back gate act more like parallel plates, but since dot 2 is closer to the tip, the tip's curvature plays a greater role in the tip capacitance–dot size relationship. The overall capacitance values are well within the expectations of finite-element electrostatic calculations, as performed in [11].

Additional insight into the properties of the QD system can be shown by examining the dI/dV signal near the Fermi level, where the STM tip functions as a transport lead in the low-bias regime. Here, electrons tunnel from the surrounding bath to the STM tip via the dot, and the charging lines intersect with peaks having the opposite slope to form diamonds near E_F , the V_b height of which (from E_F to the top of the diamond) indicates the energy difference between successive quantum dot states [27]. Examining the part of Figs. 4(b)–4(f) closest to the Fermi level, we observe diamonds whose height ranges from ≈ 6 mV on the left, where they are sometimes difficult to distinguish from noise, to up to 12–15 mV on the right. In principle the diamond height should enable a direct readout of U_2 [since the tip in Figs. 4(b)–4(f) is above dot 2] and thus remove the ambiguity of the overall energy scale from the modeling—but in the present experiment, the most visible hexagons in the charge stability diagram were located several tens of meV from the Fermi energy, so we cannot use the diamonds to assign U_2 values to each hexagonal cell and thus complete Fig. 5(f) with a plot in energy units. It is probable that in future STM experiments, higher-quality data would enable resolution of the hexagon and diamond features in the same regions of gate-bias maps, enabling a complete characterization of the system at the Hubbard-model level.

IV. CONCLUSION

We have explored a side by side DQD system in monolayer graphene under a high magnetic field. Our previous study of a single potential well system in the same material [11] showed striking and distinct single-electron charging behavior inconsistent with existing models. Here, although the interrelation between successive Landau levels is retained, the side by side dots show a tunable mergeability expected from the physical setup and capturable from the classic models of DQD systems in semiconductor devices.

ACKNOWLEDGMENTS

D.W. and F.G. acknowledge support under the Cooperative Research Agreement between the University of Maryland and the National Institute of Standards and Technology, Grant No. 70NANB14H209, and D.W. through the UMD PREP program Grant No. 70NANB23H024. T.T. and K.W. acknowl-

edge support through Japan Society for the Promotion of Science KAKENHI Grants No. 21H05233 and 23H02052, and World Premier International Research Center Initiative (WPI), Ministry of Education, culture, sports science and technology (MEXT), Japan.

APPENDIX A: EXPERIMENTAL METHODS

Data were acquired from the graphene device described in [11]. To form the double-dot system, voltages pulses spaced 100 nm apart were performed according to the following procedure: (1) stable tunneling is established at $V_{\text{bias}} = -100$ mV, $I_{\text{set}} = 40$ pA; (2) tip is raised 1.7 nm; (3) V_{bias} is ramped to 5 V at 1 V/s, held for 30 s, then ramped down. During these steps the gate voltage was set at $V_{\text{gate}} = 40$ V. V_{bias} was applied to the sample, and the tunnel current was measured from the tip (etched from a 0.25 mm Ir wire). All STM experiments were performed at 4 K, and dI/dV data were acquired using the standard lock-in technique with modulation amplitude 3 mV and frequency 1815 Hz with an 8 T applied magnetic field.

The Supplemental movies M1 and M2 [24] show slices of the dataset depicted in Figs. 3(b)–3(i), with the same color scale. Movie M1 has the same spatial axes as Figs. 3(b)–3(h), and Movie M2 has the same vertical and horizontal axes as Fig. 3(i), except that the V_g axis extends on the right to 25 V.

APPENDIX B: QUANTUM DOT MODELING

The description of the electrostatic energy model in Ref. [25] assumes that each QD is gated by only one of the two gates. When this is no longer assumed, the expressions for the dimensions of cells in the charge stability diagram become slightly more complicated, but they still allow for direct analytic solutions for the four gate capacitances given four characteristic features of the hexagonal cells: the horizontal spacing of parallel, sequential charging lines and their slope, or equivalently the horizontal and vertical spacings of these lines. First, a brief recapitulation of the expressions obtained in [25].

The total energy is calculated from $U = \frac{1}{2}(V_1 \ V_2) \begin{pmatrix} C_1 & -C_m \\ -C_m & C_2 \end{pmatrix} \begin{pmatrix} V_1 \\ V_2 \end{pmatrix}$ where the vector V represents the unknown potentials of the two dots. This vector is expressed in terms of the dot charges and gate potentials as

$$\begin{pmatrix} V_1 \\ V_2 \end{pmatrix} = \frac{1}{C_1 C_2 - C_m^2} \begin{pmatrix} C_1 & C_m \\ C_m & C_2 \end{pmatrix} \begin{pmatrix} Q_1 + S_1 \\ Q_2 + S_2 \end{pmatrix},$$

where $Q_i = -N_i e$ is the charge on the i th quantum dot and $S_i = \sum_j C_{ij} V_j$ is the weighted capacitance-voltage sum between the i th dot and the j voltage terminals, excluding the other dot. Unlike in Ref. [11] where the unusual avoidance pattern compelled us to modify Q_2 , here it is sufficient to construct the sums S_i in the same way: $S_i = C_{ig} V_g - C_{ib} V_b$, where the minus sign is caused by the bias being applied to the sample rather than the tip.

The total energy then becomes $U(N_1, N_2) = \frac{1}{2} N_1^2 U_1 + \frac{1}{2} N_2^2 U_2 + N_1 N_2 U_{12} - \frac{1}{|e|} [S_1(N_1 U_1 + N_2 U_{12}) + S_2(N_2 U_2 + N_1 U_{12})] + f(V_g, V_t)$, where f is independent of N_1 and N_2 . Then the chemical potentials are found to be

$$\mu_1 \equiv U(N_1, N_2) - U(N_1 - 1, N_2) = (N_1 - \frac{1}{2} - \frac{1}{|e|} S_1) U_1 + (N_2 - \frac{1}{|e|} S_2) U_{12}, \quad \text{and} \quad \mu_2 \equiv U(N_1, N_2) - U(N_1, N_2 - 1) = (N_2 - \frac{1}{2} - \frac{1}{|e|} S_2) U_2 + (N_1 - \frac{1}{|e|} S_1) U_{12}.$$

The charging lines of the separate dots are given by the condition $\mu_i = 0$, and the slopes of the lines can be obtained easily from the gradients of μ_i in the V_g, V_B plane:

$$\nabla \mu_1 = -\frac{1}{|e|} \begin{pmatrix} C_{1g} U_1 + C_{2g} U_{12} \\ -[C_{1r} U_1 + C_{2r} U_{12}] \end{pmatrix},$$

$$\nabla \mu_2 = -\frac{1}{|e|} \begin{pmatrix} C_{2g} U_2 + C_{1g} U_{12} \\ -[C_{2r} U_2 + C_{1r} U_{12}] \end{pmatrix}.$$

Then the corresponding slopes are $m_1 = \frac{C_{1g} + C_{2g} \gamma_1}{C_{1r} + C_{2r} \gamma_1}$, $m_2 = \frac{C_{2g} + C_{1g} \gamma_2}{C_{2r} + C_{1r} \gamma_2}$, where $\gamma_i \equiv \frac{U_{12}}{U_i}$ is the coupling parameter which goes to unity in the limit of merged dots. (Note that in this limit, the slopes become identical.) The horizontal

spacing of parallel charging lines is determined by the following conditions (for dots 1 and 2, respectively):

$$\mu_1(N_1 + 1, N_2, V_g + \Delta V_{g1}) = \mu_1(N_1, N_2, V_g),$$

$$\mu_2(N_1, N_2 + 1, V_g + \Delta V_{g2}) = \mu_2(N_1, N_2, V_g),$$

and these conditions yield $\Delta V_{g1} = |e|/(C_{1g} + C_{2g} \gamma_1)$, $\Delta V_{g2} = |e|/(C_{2g} + C_{1g} \gamma_2)$. Finally, we have the conditions for the horizontal shift of one dot's charging line from charging the other dot, denoted ΔV_{gi}^m and obtained from

$$\mu_1(N_1, N_2 + 1, V_g + \Delta V_{g1}^m) = \mu_1(N_1, N_2, V_g),$$

$$\mu_2(N_1 + 1, N_2, V_g + \Delta V_{g2}^m) = \mu_2(N_1, N_2, V_g),$$

resulting in $\Delta V_{g1}^m = \gamma_1 \Delta V_{g1}$, $\Delta V_{g2}^m = \gamma_2 \Delta V_{g2}$; this result is identical to Ref. [25]. These six equations are sufficient to obtain the six constants $\gamma_1, \gamma_2, C_{1g}, C_{2g}, C_{1r}, C_{2r}$ from the dimensions of cells measured from $\frac{dI}{dV}(V_g, V_B)$ maps, appearing in Fig. 5. (Due to the definitions of U_1, U_2, U_{12} within the capacitive model, $\gamma_i \equiv \frac{U_{12}}{U_i} = C_m/C_{3-i}$.)

-
- [1] J. Velasco, L. Ju, D. Wong, S. Kahn, J. Lee, H.-Z. Tsai, C. Germany, S. Wickenburg, J. Lu, T. Taniguchi, K. Watanabe, A. Zettl, F. Wang, and M. F. Crommie, Nanoscale control of rewriteable doping patterns in pristine graphene/boron nitride heterostructures, *Nano Lett.* **16**, 1620 (2016).
- [2] L. Ju, J. Velasco, E. Huang, S. Kahn, C. Nosioglia, H.-Z. Tsai, W. Yang, T. Taniguchi, K. Watanabe, Y. Zhang, G. Zhang, M. Crommie, A. Zettl, and F. Wang, Photoinduced doping in heterostructures of graphene and boron nitride, *Nat. Nanotechnol.* **9**, 348 (2014).
- [3] W. Shi, S. Kahn, L. Jiang, S.-Y. Wang, H.-Z. Tsai, D. Wong, T. Taniguchi, K. Watanabe, F. Wang, M. F. Crommie, and A. Zettl, Reversible writing of high-mobility and high-carrier-density doping patterns in two-dimensional van der Waals heterostructures, *Nat. Electron.* **3**, 99 (2020).
- [4] Z. Ge, S. Slizovskiy, P. Polizogopoulos, T. Joshi, T. Taniguchi, K. Watanabe, D. Lederman, V. I. Fal'ko, and J. Velasco, Giant orbital magnetic moments and paramagnetic shift in artificial relativistic atoms and molecules, *Nat. Nanotechnol.* **18**, 250 (2023).
- [5] Z. J. Krebs, W. A. Behn, S. Li, K. J. Smith, K. Watanabe, T. Taniguchi, A. Levchenko, and V. W. Brar, Imaging the breaking of electrostatic dams in graphene for ballistic and viscous fluids, *Science* **379**, 671 (2023).
- [6] J. Velasco Jr., J. Lee, D. Wong, S. Kahn, H.-Z. Tsai, J. Costello, T. Umeda, T. Taniguchi, K. Watanabe, A. Zettl, F. Wang, and M. F. Crommie, Visualization and control of single electron charging in bilayer graphene quantum dots, *Nano Lett.* **18**, 5104 (2018).
- [7] J. F. Rodriguez-Nieva and L. S. Levitov, Berry phase jumps and giant nonreciprocity in Dirac quantum dots, *Phys. Rev. B* **94**, 235406 (2016).
- [8] F. Ghahari, D. Walkup, C. Gutiérrez, J. F. Rodriguez-Nieva, Y. Zhao, J. Wyrick, F. D. Natterer, W. G. Cullen, K. Watanabe, T. Taniguchi, L. S. Levitov, N. B. Zhitenev, and J. A. Stroscio, An on/off Berry phase switch in circular graphene resonators, *Science* **356**, 845 (2017).
- [9] D. Walkup and J. A. Stroscio, Helical level structure of Dirac potential wells, *Phys. Rev. B* **96**, 201409(R) (2017).
- [10] C. Gutiérrez, D. Walkup, F. Ghahari, C. Lewandowski, J. F. Rodriguez-Nieva, K. Watanabe, T. Taniguchi, L. S. Levitov, N. B. Zhitenev, and J. A. Stroscio, Interaction-driven quantum Hall wedding cake-like structures in graphene quantum dots, *Science* **361**, 789 (2018).
- [11] D. Walkup, F. Ghahari, C. Gutiérrez, K. Watanabe, T. Taniguchi, N. B. Zhitenev, and J. A. Stroscio, Tuning single-electron charging and interactions between compressible Landau level islands in graphene, *Phys. Rev. B* **101**, 035428 (2020).
- [12] C. Livermore, C. H. Crouch, R. M. Westervelt, K. L. Campman, and A. C. Gossard, The Coulomb blockade in coupled quantum dots, *Science* **274**, 1332 (1996).
- [13] K. A. Matveev, L. I. Glazman, and H. U. Baranger, Coulomb blockade of tunneling through a double quantum dot, *Phys. Rev. B* **54**, 5637 (1996).
- [14] Y. Zhao, J. Wyrick, F. D. Natterer, J. F. Rodriguez-Nieva, C. Lewandowski, K. Watanabe, T. Taniguchi, L. S. Levitov, N. B. Zhitenev, and J. A. Stroscio, Creating and probing electron whispering-gallery modes in graphene, *Science* **348**, 672 (2015).
- [15] N. M. Freitag, L. A. Chizhova, P. Nemes-Incze, C. R. Woods, R. V. Gorbachev, Y. Cao, A. K. Geim, K. S. Novoselov, J. Burgdörfer, F. Libisch, and M. Morgenstern, Electrostatically confined monolayer graphene quantum dots with orbital and valley splittings, *Nano Lett.* **16**, 5798 (2016).
- [16] M. T. Woodside and P. L. McEuen, Scanned probe imaging of single-electron charge states in nanotube quantum dots, *Science* **296**, 1098 (2002).
- [17] J. Tersoff and D. R. Hamann, Theory of the scanning tunneling microscope, *Phys. Rev. B* **31**, 805 (1985).
- [18] C. J. Chen, Theory of scanning tunneling spectroscopy, *J. Vac. Sci. Technol., A* **6**, 319 (1988).
- [19] K. Teichmann, M. Wenderoth, S. Loth, R. G. Ulbrich, J. K. Garleff, A. P. Wijnheijmer, and P. M. Koenraad, Controlled

- charge switching on a single donor with a scanning tunneling microscope, *Phys. Rev. Lett.* **101**, 076103 (2008).
- [20] F. Marczinowski, J. Wiebe, F. Meier, K. Hashimoto, and R. Wiesendanger, Effect of charge manipulation on scanning tunneling spectra of single Mn acceptors in InAs, *Phys. Rev. B* **77**, 115318 (2008).
- [21] J. Wyrick, F. D. Natterer, Y. Zhao, K. Watanabe, T. Taniguchi, W. G. Cullen, N. B. Zhitenev, and J. A. Stroscio, Tomography of a probe potential using atomic sensors on graphene, *ACS Nano* **10**, 10698 (2016).
- [22] J. M. Elzerman, R. Hanson, J. S. Greidanus, L. H. Willems van Beveren, S. De Franceschi, L. M. K. Vandersypen, S. Tarucha, and L. P. Kouwenhoven, Few-electron quantum dot circuit with integrated charge read out, *Phys. Rev. B* **67**, 161308(R) (2003).
- [23] S. Jung, G. M. Rutter, N. N. Klimov, D. B. Newell, I. Calizo, A. R. Hight-Walker, N. B. Zhitenev, and J. A. Stroscio, Evolution of microscopic localization in graphene in a magnetic field from scattering resonances to quantum dots, *Nat. Phys.* **7**, 245 (2011).
- [24] See Supplemental Material at <http://link.aps.org/supplemental/10.1103/PhysRevB.108.235407> for movies M1 and M2 representing the complete 3D image.
- [25] W. G. van der Wiel, S. De Franceschi, J. M. Elzerman, T. Fujisawa, S. Tarucha, and L. P. Kouwenhoven, Electron transport through double quantum dots, *Rev. Mod. Phys.* **75**, 1 (2002).
- [26] S. Yang, X. Wang, and S. Das Sarma, Generic Hubbard model description of semiconductor quantum-dot spin qubits, *Phys. Rev. B* **83**, 161301(R) (2011).
- [27] R. Hanson, L. P. Kouwenhoven, J. R. Petta, S. Tarucha, and L. M. K. Vandersypen, Spins in few-electron quantum dots, *Rev. Mod. Phys.* **79**, 1217 (2007).
- [28] S. Das Sarma, X. Wang, and S. Yang, Hubbard model description of silicon spin qubits: Charge stability diagram and tunnel coupling in Si double quantum dots, *Phys. Rev. B* **83**, 235314 (2011).
- [29] J. M. Golden and B. I. Halperin, Relation between barrier conductance and Coulomb blockade peak splitting for tunnel-coupled quantum dots, *Phys. Rev. B* **53**, 3893 (1996).